PCCP

PAPER

View Article Online
View Journal | View Issue

Check for updates

Cite this: *Phys. Chem. Chem. Phys.*, 2017, **19**, 27059

Self-assembled bundled TiO_2 nanowire arrays encapsulated with indium tin oxide for broadband absorption in plasmonic photocatalysis

Hao Huang,[ab] Qi Hao,[ab] Xingce Fan,[a] Zhengwei Luo,[a] Xiangyu Hou,[a]
Xiaozhi Yang,[a] Teng Qiu*[a] and Paul K. Chu*[b]

Received 22nd June 2017,
Accepted 13th September 2017

DOI: 10.1039/c7cp04196a

rsc.li/pccp

In order to enhance photocatalysis by broadening light harvesting, bundled TiO_2 nanowire bundle arrays are encapsulated with indium tin oxide (ITO) by a self-assembly technique involving anodization, electrochemical etching, and ITO deposition. The plasmonic photocatalyst, which has a multiscale structure with variable nanoscale gaps as well as microscale funnels, shows broadband localized surface plasmon resonance absorption of 84% in the wavelength range between 400 and 2500 nm. The improved photocatalytic efficiency is demonstrated by methyl orange degradation under sunlight illumination. The improvement stems from enhanced light harvesting arising from the localized surface plasmon resonance of the ITO membrane which extends the light response to the visible and NIR regions and excites hot charge carriers.

1. Introduction

Titanium dioxide (TiO_2) is an extensively studied semiconductor in photocatalysis due to its promising performance in applications including decomposition of toxic organics,[1–3] hydrogen evolution from water splitting,[4–6] and photo-induced carbon dioxide reduction.[7–10] Nevertheless, the large bandgap of TiO_2 ($\sim$3.2 eV) limits its photo-absorption to the ultraviolet (UV) region, which only accounts for about 4% of the total solar energy.[11,12] Hence, semiconductor photocatalysts that can harvest a wide spectrum of solar light for efficient solar energy conversion is crucial to photocatalysis. Several strategies such as doping with nonmetals (NO_x and N)[13–16] or metals (Cr and V)[17–19] and construction of heterojunctions[20–22] have been proposed to extend the absorption of TiO_2 to visible light. However, the doped materials typically suffer from thermal instability, photocorrosion, and fast e^-/h^+ recombination rates, thereby limiting their photocatalytic efficiency. Moreover, near-infrared (NIR) light, which accounts for 50% of the solar spectrum, is barely utilized. Consequently, there is much interest in developing efficient photocatalysts with a wide absorption range spanning UV to NIR.

Plasmonic photocatalysts composed of plasmonic materials and semiconductors have attracted increasing interest because of their excellent optical absorption from the visible to NIR regions and superior photocatalytic performance.[23–27] Plasmonic photocatalysis benefits from localized surface plasmon resonance (LSPR) which represents the strong oscillation of the free electrons on the surface of plasmonic materials in phase with the varying electric field of the incident light. There are three strategies to extend the photocatalytic performance of plasmonic photocatalysts to the visible and NIR light range. Firstly, the plasmonic materials can be directly coupled to semiconductors so that the photogenerated electrons or holes from LSPR absorption may be transferred to the semiconductors.[28] Secondly, the excited plasmonic components can also transfer the absorbed energy to semiconductors radiatively through the localized interactions between the semiconductors and the LSPR-induced enhanced localized electric field.[23] The third one is that heat generated from LSPR absorption to the surroundings due to nonradiative decay of surface plasmons to phonons can accelerate the photocatalytic reactions by increasing the local temperature around the semiconductors.[29]

In order to maximize the plasmonic effects in the TiO_2 photocatalytic performance, the plasmonic materials are expected to provide good overlap between the LSPR absorption band and incident light. The resonant wavelength and LSPR intensity depend not only on the nature of the plasmonic materials, but also the size and shape of the nanostructures.[30–33] By manipulating the composition and morphology of the plasmonic materials, it is possible to design nanostructures that interact with the broad solar spectrum.[34,35] Among the different plasmonic photocatalysts, much attention has been paid to harvesting visible

---

[a] *School of Physics, Southeast University, Nanjing 211189, People's Republic of China. E-mail: tqiu@seu.edu.cn*

[b] *Department of Physics and Materials Science, City University of Hong Kong, Tat Chee Avenue, Kowloon, Hong Kong, China. E-mail: paul.chu@cityu.edu.hk*

light from metallic nanoparticles (Ag: *ca.* 410 nm, Au: *ca.* 520 nm),[24] but there has been less effort to harvest long-wavelength light which actually accounts for a larger proportion of solar energy.[36,37] Indium tin oxide (ITO) with tunable LSPR absorption in the NIR region is a possible candidate.[38] ITO is a transparent, conducting oxide typically consisting of 90 wt% indium oxide (In_2O_3) and 10 wt% tin oxide (SnO_2). Compared to noble-metal nanostructures, ITO possesses excellent chemical stability and losses are quite small at NIR and at longer wavelengths.[39] Herein, we describe a strategy to achieve wide-range visible-NIR light harvesting in TiO_2. The materials are prepared by introducing ITO nanoparticles on a bundled nanowire array (BNWA) using a bottom-up self-assembly approach that combines anodization and electric-field-directed electrochemical etching. The ITO-BNWA plasmonic photocatalyst has multiscale structures with a small taper angle and varying nanogaps between aggregated nanowires. Broadband absorption with an average absorption of 84% in the wavelength range between 400 and 2500 nm is achieved. The photocatalytic activity is further evaluated by means of methyl orange (MO) degradation under solar light illumination and is compared to that of intrinsic TiO_2.

2. Experimental details

2.1 Fabrication of bundled TiO_2 nanowire arrays

Prior to anodization, the high-purity titanium (Ti) foils (99.7%, 30 mm × 30 mm × 0.5 mm in size) were ultrasonically cleaned in acetone, ethanol, and distilled water for 10 min each. Chemical polishing was then carried out for 5 min in a mixture of hydrofluoric acid (40 wt%), nitric acid (65 wt%), and water with a volume ratio of 1 : 4 : 5 to further remove surface impurities, followed by rinsing in distilled water and drying in N_2.

The BNWAs were prepared by potentiostatic anodization of the Ti foil (with an exposed area of 2.5 cm^2) in a two-electrode electrochemical cell with platinum foil as the cathode and Ti foil as the anode. Anodization was carried out in an electrolyte containing ammonium fluoride (NH_4F, 0.9 wt%), water (3 vol%), and ethylene glycol (EG) at 60 V and room temperature. The distance between the two electrodes was 2 cm. After anodization for 1.5 h, the samples were cleaned with distilled water immediately, dried with N_2, and annealed in air at 400 °C for 0.5 h.

2.2 Deposition of the ITO film

The ITO (10% Sn-doped) films were prepared using BNWAs by the magnetron sputtering system (ATC orion sputtering system) in an oxygen/argon plasma with a ratio at 1 : 32 at room temperature. The magnetron power was 60 W. During deposition, the pressure in the chamber was 0.5 Pa and the distance between the target and the substrate was 10 cm. The deposition rate was calculated to be 0.71 nm s^{-1}. In order to improve crystallization, the samples were annealed at 400 °C for 0.5 h under vacuum.

2.3 Characterization

Scanning electron microscopy (SEM, FEI Inspect F50) was used to examine the morphology of the nanocomposites and X-ray diffraction (XRD, Smartlab, Cu Kα1) was performed to investigate the crystal structure. Transmission electron microscopic (TEM) images and high resolution transmission electron microscopic (HRTEM) images were acquired using a FEI Tecnai G20. An ultra-violet visible near infra-red spectrophotometer with a 60 nm diameter integrating sphere (PE Lamda 750) was employed in the hemispherical reflectance measurements in the UV-Vis-NIR range (200 nm to 2.5 μm). A Fourier transform infrared spectrometer (PE Spectrum 100) with specular transmittance and reflectance accessories was used to acquire spectra in the mid-infrared regime (400 to 4000 cm^{-1}) with a resolution of 4 cm^{-1}.

2.4 Evaluation of photocatalytic activity

The photocatalytic activity of the BNWA was evaluated by photo-decomposition of methyl orange (MO) under light irradiation using a solar simulator (ABET Technologies Sun 2000) at room temperature. The sample was put in 5 mL of an MO aqueous solution with a concentration of 2.5×10^{-4} M in a 10 mL beaker. The active area of the photocatalyst was about 2.5 cm^2 (Φ 1.8 cm). Prior to irradiation, the system was kept in the dark for 30 min to establish the adsorption/desorption equilibrium between the dye and the photocatalyst under ambient conditions. At given irradiation intervals, the solution was collected for analysis. The residual MO concentration was determined by UV-Vis spectrophotometry (HALO DB-20S).

3. Results and discussion

As shown in Fig. 1, self-aggregated bundled TiO_2 nanowire arrays are formed by a simple anodization process in ethylene glycol (EG) containing NH_4F and water. Fig. 1a shows that the BNWA covering the entire surface has an average diameter of 50 nm and a length of around 6 μm. The thicknesses of the double layer structure of the top nanowires and bottom nanotubes are 2 μm and 14 μm, respectively, according to the cross-sectional SEM image in Fig. 1b. The nanowires are formed by field-assisted electrochemical etching and chemical dissolution at the mouth of the tubes as shown in the following:[40]

$$\text{Field-assisted etching: } TiO_2 + 6F^- + 4H^+ \rightarrow [TiF_6]^{2-} + 2H_2O$$

and

$$\text{Chemical dissolution: } TiO_2 + 6HF \rightarrow [TiF_6]^{2-} + 2H_2O + 2H^+.$$

Owing to the presence of F^- and H^+ at the mouth of the nanotubes, field-assisted etching occurs at the statistically distributed "breakdown sites", similar to the pitting process in the initial stage of anodization of TiO_2 nanotubes. As anodization proceeds, the nanotubes split along the vertical tube axis to form nanowires from the top as shown in Fig. 1d. After anodization, the sample is taken out, washed with distilled water, and dried under flowing N_2. In the drying process, if the water–air surface tension between the two TiO_2 nanowires exceeds the stiffness of the nanowires, the nanowires will bend towards the surrounding nanowires. If this bending force is

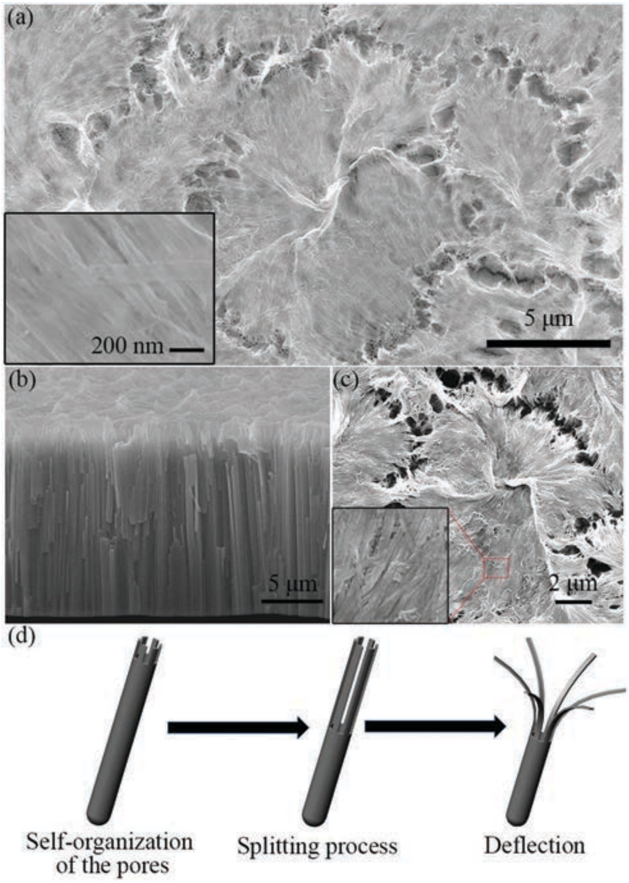

Fig. 1 Representative SEM images of the BNWA prepared by anodization of Ti foils: (a) overview of nanowire bundles, with the inset showing the magnified view of the nanowires; (b) cross-sectional view of (a); (c) top view of the ITO encapsulated BNWA, with the inset showing the magnified view of the ITO encapsulated nanowires; (d) schematic diagram of the mechanism of the formation of nanowires on the anodic TiO_2 nanotube arrays.

greater than the yield strength, the bending nanowires will plastically collapse, resulting in the formation of self-aggregated nanowire bundles.[41] Because the surface tension has a random direction, the BNWA shows an irregular three-dimensional (3D) pattern resembling mountain ridges and valleys, as shown in the SEM images in Fig. 1a. On top of the structure, an ITO film with 30 nm thickness is sputter-deposited after annealing and the bundled nanowire structure still exists as shown in Fig. 1c. It is noted that the film is black in color.

To understand and analyze the plasmonic modes of the nanostructured ITO membrane, the shape and size of the collapsed TiO_2 nanowires before ITO coating are determined. Fig. 2a shows that TiO_2 nanotubes with a diameter of about 120 nm exist underneath the nanowire layer and the bottom ends of the nanowires are mechanically connected to the mouth of the nanotubes. The cross-sectional SEM image of the BNWA in Fig. 2b shows that the self-aggregated bundle has the shape of a concave funnel with an average inclined angle of 30°, a height of 2.9 μm, and a width of 5 μm.

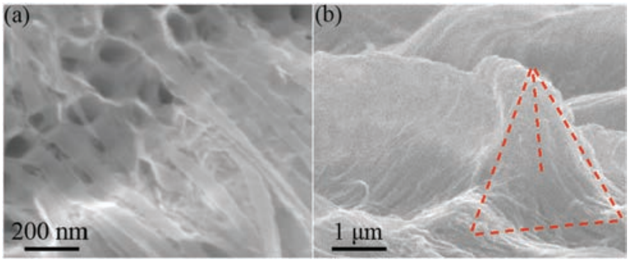

Fig. 2 SEM images of the nanostructure: (a) collapsed TiO_2 nanowires linked to the vertices of the nanotube unit on the bottom; (b) typical cross-sectional view of the ITO membrane showing funnel-shaped bundles, in which the red dashed line indicates the outline of the cross-section of a TiO_2 nanowire bundle. Scale bars, (a) 200 nm and (b) 1 μm, respectively.

The ITO encapsulated TiO_2 nanowire structure can be clearly observed in the TEM image in Fig. 3(a). Fig. 3(b) shows the HRTEM diffraction fringe pattern with lattice spacings of 0.350 nm and 0.270 nm corresponding to the (101) plane of TiO_2 and the (321) plane of ITO, respectively. XRD is performed to investigate the crystalline phase and the crystal structure of the as-prepared and ITO coated BNWAs. The as-prepared BNWA is amorphous and no diffraction peaks associated with crystalline TiO_2 are detected (Fig. 3c). The salient diffraction peaks of the annealed sample are associated with crystallized ITO and anatase TiO_2 except those arising from the underlying Ti substrate. The sharp peaks at $2\theta = 37^\circ$ and 48° are indexed to the TiO_2 anatase phases (103)

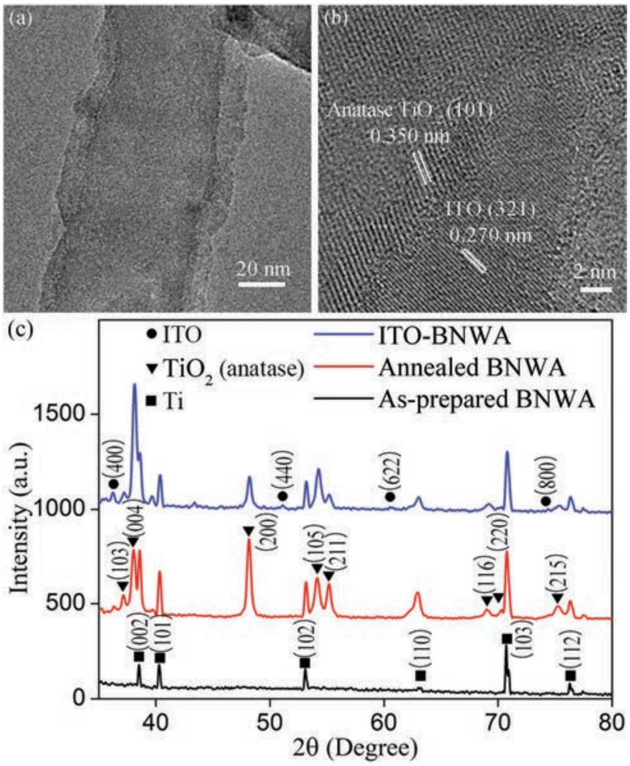

Fig. 3 (a) TEM image and (b) HRTEM image of the ITO encapsulated BNWA; (c) XRD spectra of the as-prepared, annealed and ITO encapsulated BNWA.

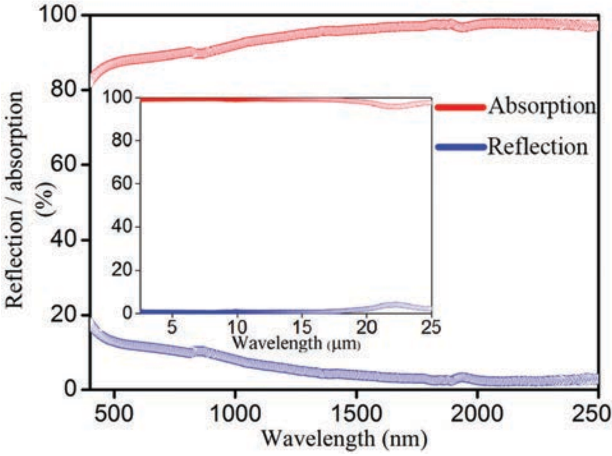

Fig. 4 Reflection and absorption spectra of the black plasmonic composite photocatalyst ITO-BNWA.

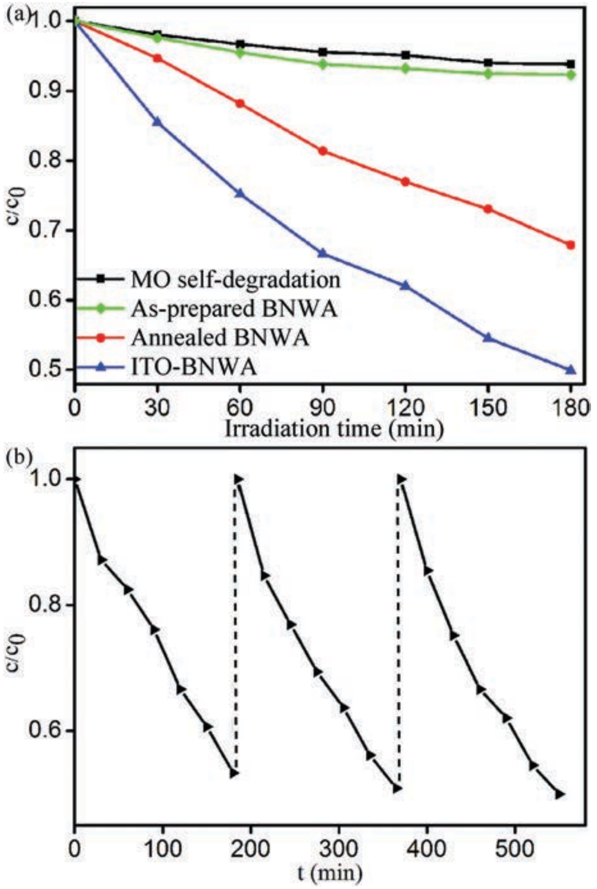

Fig. 5 (a) Self-degradation of MO under solar light irradiation and photocatalytic degradation of the as-prepared, annealed and ITO encapsulated BNWA; (b) stability in the ITO-BNWA photocatalytic degradation of MO after three cycles.

and (200). Anatase is generally recognized to be the most active in photocatalysis among the common crystal phases of TiO_2.[42–44] There are weak diffraction peaks associated with ITO at 2θ = 35.5°, 50.9°, 60.7°, and 74.4°. These patterns match the diffraction patterns of the (400), (440), (622) and (800) planes of cubic crystalline ITO.

Fig. 4 shows the reflection and absorption spectra of the ITO-BNWA. The membrane has broadband absorption properties and low reflection of less than ~6% in the range of 400–2500 nm. The reflection spectrum in the mid-infrared region is displayed in the inset of Fig. 4 and the average reflection is as low as ~3% in the range of 2.5–25 μm. Broadband absorption originates from the multiple LSPR modes of the ITO film, multiple nanoscale gaps with a depth of a few micrometers, as well as the microscale funnel shape. ITO is a conducting metal oxide consisting of a metal oxide semiconductor, In_2O_3, doped with a group IV element, Sn. Sn provides free charge carriers that are responsible for the LSPR effect, which is phenomenologically the same as that observed from noble metals. The density of free charge carriers in ITO ($n \approx 10^{21}$ electrons per cm^3) is smaller than that of noble metals ($n \approx 10^{23}$ electrons per cm^3)[45] and as a result, the intrinsic LSPR absorption of ITO appears at longer wavelengths in the NIR region. LSPR absorption is determined by not only the properties but also the morphological features of the plasmonic materials. Here, the TiO_2 nanowires collapse and aggregate in arbitrary directions to form the membrane. The ITO structure is still aligned with the BNWA after sputter-coating. The ridges and valleys are randomly distributed and the cross sections have a common funnel shape. The inhomogeneous morphology supports the LSPR modes over a wide wavelength range giving rise to broadband light absorption. Furthermore, increasing the photon path length in the surface region of TiO_2 due to multiple scattering in the ITO film enhances optical absorption.

To evaluate the photocatalytic activity, MO photocatalytic degradation experiments are performed under solar light illumination. The absorption spectra of the aqueous MO are monitored for over 3 h and the change in the intensity of the MO absorption peak at λ = 463.5 nm is used to determine the decay rates by fitting the data to c/c_0, where c_0 and c are the absorbance of MO at time t = 0 and t (t denoting the reaction time). Fig. 5a shows the comparison among the amorphous, annealed, and ITO encapsulated BNWA. Photocatalytic activity is barely observed from the pristine amorphous BNWA because of the low absorption ratio of solar light. On the other hand, the degradation rate of the annealed samples with ITO increases significantly and generally, the photocatalytic efficiency can be estimated by the following first-order kinetics equation:

$$\kappa = -\ln(c/c_0)/t,$$

where κ is the reaction rate. Additionally, the durability of a photocatalyst is crucial and the stability is assessed by cycling experiments (Fig. 5b). After three cycles of photocatalytic degradation of MO, the catalyst does not exhibit any significant loss of efficiency confirming the stability.

Two mechanisms are responsible for the enhanced photocatalytic activity. The first one is charge carrier injection from ITO to TiO_2 and the second one is energy transfer from excited ITO LSPR to TiO_2. The addition of Sn donor impurities contributes

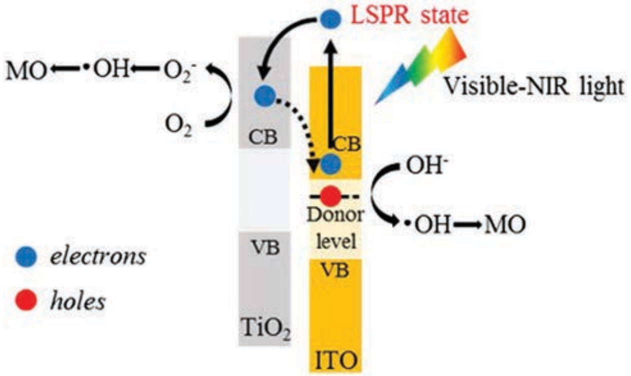

Fig. 6 Schematic illustration of photocatalytic degradation of MO on ITO-BNWA due to the LSPR effect of ITO under visible and NIR light irradiation.

electron energy levels high in the semiconductor band gap so that electrons can be easily excited into the conduction band. Since LSPR is induced by electromagnetic radiation, the ITO film drives collective electron oscillations. Non-radiative relaxation of plasmons transfers the incident photon energy to hot electrons which acquire sufficient energy and momentum to overcome the heterojunction barrier at the ITO–TiO_2 interface[46,47] (see Fig. 6). The injected electrons then reduce dissolved oxygen adsorbed on the surface of TiO_2 to form •OH radicals *via* chain reactions.[48] Electron injection from the ITO film into the conduction band of TiO_2 leaves a positive charge (hole) on the conduction band of ITO which can be neutralized by electron-donating species in the solution. The holes that transfer to the surface of the ITO film and •OH radicals originating from electro-reduction of dissolved oxygen with electrons are the major reactive oxygen species responsible for MO degradation.[49] Although the heterojunction between the ITO and the TiO_2 may enable electrons in the conduction band of TiO_2 to transfer back to ITO as shown by the dashed line in Fig. 6, the intensive LSPR effect still dominates in the migration of electrons resulting in continuous hot electron injection into TiO_2. Meanwhile, the ITO film produces heat under optical illumination due to nonradiative decay of surface plasmons into phonon modes.[50] Localized heating and the ensuing temperature increase further enhance the photocatalytic activity by increasing the redox reaction rate and mass transfer.

4. Conclusion

Broadband visible-NIR light harvesting is achieved by encapsulating the bundled nanowire array (BNWA) with TiO_2. The nanostructured BNWAs are fabricated by anodization of titanium foils in EG + NH_4F. The TiO_2 nanowires produced by vertical splitting of the anodically grown nanotubes collapse into bundles due to surface tension in the drying process. After ITO sputter-coating and annealing, the ITO encapsulated BNWAs show a random 3D pattern of ridges and valleys and a cross section with a microscale funnel shape. The bundles have a multiscale structure and variable ITO nanoscale gaps ranging from zero to hundreds of nanometers over a depth of a few microns and the microscale funnel structure leads to broadband absorption. The plasmonic photocatalyst shows an average absorption efficiency of 84% in the wavelength range between 400 and 2500 nm, a solar light photocatalytic activity enhancement of 50%, and good stability due to localized surface plasmon resonance absorption of ITO under solar light irradiation and charge separation at the ITO layer. The ITO-BNWA plasmonic photocatalyst with broadband absorption spanning the visible and mid-infrared regions has great potential in efficient harvesting of sunlight in photocatalytic applications.

Conflicts of interest

There are no conflicts of interest to declare.

Acknowledgements

This work was supported by the National Key R&D Program of China (Grant No. 2017YFA0403600), City University of Hong Kong Applied Research Grant (ARG) No. 9667122 and Strategic Research Grant (SRG) No. 7004644.

References

1 R. Asahi, T. Morikawa, T. Ohwaki, K. Aoki and Y. Taga, *Science*, 2001, **293**, 269–271.
2 S. X. Ouyang and J. H. Ye, *J. Am. Chem. Soc.*, 2011, **133**, 7757–7763.
3 J. W. Tang, Z. G. Zou and J. H. Ye, *Angew. Chem., Int. Ed.*, 2004, **43**, 4463–4466.
4 A. Fujishima and K. Honda, *Nature*, 1972, **238**, 37–38.
5 P. Szymanski and M. A. El-Sayed, *Theor. Chem. Acc.*, 2012, **131**, 1202.
6 M. Ni, M. K. H. Leung, D. Y. C. Leung and K. Sumathy, *Renewable Sustainable Energy Rev.*, 2007, **11**, 401–425.
7 V. P. Indrakanti, H. H. Schobert and J. D. Kubicki, *Energy Fuels*, 2009, **23**, 5247–5256.
8 T. Inoue, A. Fujishima, S. Konishi and K. Honda, *Nature*, 1979, **277**, 637–638.
9 K. Koci, L. Obalova and Z. Lacny, *Chem. Pap.*, 2008, **62**, 1–9.
10 S. C. Roy, O. K. Varghese, M. Paulose and C. A. Grimes, *ACS Nano*, 2010, **4**, 1259–1278.
11 M. Murdoch, G. I. N. Waterhouse, M. A. Nadeem, J. B. Metson, M. A. Keane, R. F. Howe, J. Llorca and H. Idriss, *Nat. Chem.*, 2011, **3**, 489–492.
12 A. Hagfeldt and M. Gratzel, *Chem. Rev.*, 1995, **95**, 49–68.
13 X. B. Chen, L. Liu, P. Y. Yu and S. S. Mao, *Science*, 2011, **331**, 746–750.
14 S. U. M. Khan, M. Al-Shahry and W. B. Ingler, *Science*, 2002, **297**, 2243–2245.
15 W. J. Ren, Z. H. Ai, F. L. Jia, L. Z. Zhang, X. X. Fan and Z. G. Zou, *Appl. Catal., B*, 2007, **69**, 138–144.

16 S. Sakthivel and H. Kisch, *Angew. Chem., Int. Ed.*, 2003, **42**, 4908–4911.

17 S. Klosek and D. Raftery, *J. Phys. Chem. B*, 2001, **105**, 2815–2819.

18 W. Y. Choi, A. Termin and M. R. Hoffmann, *J. Phys. Chem.*, 1994, **98**, 13669–13679.

19 E. Borgarello, J. Kiwi, M. Gratzel, E. Pelizzetti and M. Visca, *J. Am. Chem. Soc.*, 1982, **104**, 2996–3002.

20 Y. Bessekhouad, D. Robert and J. Weber, *J. Photochem. Photobiol., A*, 2004, **163**, 569–580.

21 Y. Bessekhouad, D. Robert and J. V. Weber, *Catal. Today*, 2005, **101**, 315–321.

22 G. Marci, V. Augugliaro, M. J. Lopez-Munoz, C. Martin, L. Palmisano, V. Rives, M. Schiavello, R. J. D. Tilley and A. M. Venezia, *J. Phys. Chem. B*, 2001, **105**, 1026–1032.

23 K. Awazu, M. Fujimaki, C. Rockstuhl, J. Tominaga, H. Murakami, Y. Ohki, N. Yoshida and T. Watanabe, *J. Am. Chem. Soc.*, 2008, **130**, 1676–1680.

24 S. Linic, P. Christopher and D. B. Ingram, *Nat. Mater.*, 2011, **10**, 911–921.

25 L. Q. Liu, S. X. Ouyang and J. H. Ye, *Angew. Chem., Int. Ed.*, 2013, **52**, 6689–6693.

26 Q. Hao, C. X. Wang, H. Huang, W. Li, D. Y. Du, D. Han, T. Qiu and P. K. Chu, *Sci. Rep.*, 2015, **5**, 15288.

27 H. Huang, X. C. Fan, Q. Hao, D. Y. Du, X. G. Luo and T. Qiu, *RSC Adv.*, 2016, **6**, 12611–12615.

28 Y. Tian and T. Tatsuma, *J. Am. Chem. Soc.*, 2005, **127**, 7632–7637.

29 X. Chen, Z. F. Zheng, X. B. Ke, E. Jaatinen, T. F. Xie, D. J. Wang, C. Guo, J. C. Zhao and H. Y. Zhu, *Green Chem.*, 2010, **12**, 414–419.

30 L. Brus, *Acc. Chem. Res.*, 2008, **41**, 1742–1749.

31 C. Burda, X. B. Chen, R. Narayanan and M. A. El-Sayed, *Chem. Rev.*, 2005, **105**, 1025–1102.

32 M. A. El-Sayed, *Acc. Chem. Res.*, 2001, **34**, 257–264.

33 K. L. Kelly, E. Coronado, L. L. Zhao and G. C. Schatz, *J. Phys. Chem. B*, 2003, **107**, 668–677.

34 M. Rycenga, C. M. Cobley, J. Zeng, W. Y. Li, C. H. Moran, Q. Zhang, D. Qin and Y. N. Xia, *Chem. Rev.*, 2011, **111**, 3669–3712.

35 Y. N. Xia, Y. J. Xiong, B. Lim and S. E. Skrabalak, *Angew. Chem., Int. Ed.*, 2009, **48**, 60–103.

36 J. Lee, S. Mubeen, X. L. Ji, G. D. Stucky and M. Moskovits, *Nano Lett.*, 2012, **12**, 5014–5019.

37 Y. Q. Qu, R. Cheng, Q. Su and X. F. Duan, *J. Am. Chem. Soc.*, 2011, **133**, 16730–16733.

38 M. Kanehara, H. Koike, T. Yoshinaga and T. Teranishi, *J. Am. Chem. Soc.*, 2009, **131**, 17736–17737.

39 P. R. West, S. Ishii, G. V. Naik, N. K. Emani, V. M. Shalaev and A. Boltasseva, *Laser Photonics Rev.*, 2010, **4**, 795–808.

40 J. H. Lim and J. Choi, *Small*, 2007, **3**, 1504–1507.

41 J. J. Hill, K. Haller, B. Gelfand and K. J. Ziegler, *ACS Appl. Mater. Interfaces*, 2010, **2**, 1992–1998.

42 K. Lee, D. Kim, P. Roy, I. Paramasivam, B. I. Birajdar, E. Spiecker and P. Schmuki, *J. Am. Chem. Soc.*, 2010, **132**, 1478–1479.

43 G. Liu, J. C. Yu, G. Q. Lu and H. M. Cheng, *Chem. Commun.*, 2011, **47**, 6763–6783.

44 K. Yanagisawa and J. Ovenstone, *J. Phys. Chem. B*, 1999, **103**, 7781–7787.

45 M. D. Losego, A. Y. Efremenko, C. L. Rhodes, M. G. Cerruti, S. Franzen and J. P. Maria, *J. Appl. Phys.*, 2009, **106**, 024903.

46 S. Mubeen, G. Hernandez-Sosa, D. Moses, J. Lee and M. Moskovits, *Nano Lett.*, 2011, **11**, 5548–5552.

47 C. Ng, J. J. Cadusch, S. Dligatch, A. Roberts, T. J. Davis, P. Mulvaney and D. E. Gomez, *ACS Nano*, 2016, **10**, 4704–4711.

48 Y. Lu, H. T. Yu, S. Chen, X. Quan and H. M. Zhao, *Environ. Sci. Technol.*, 2012, **46**, 1724–1730.

49 Y. M. Wu, H. B. Liti, J. L. Zhang and F. Chen, *J. Phys. Chem. C*, 2009, **113**, 14689–14695.

50 K. Bae, G. Kang, S. K. Cho, W. Park, K. Kim and W. J. Padilla, *Nat. Commun.*, 2015, **6**, 10103.